Thermal conductivity of metal coated polymer foam: Integrated experimental and modeling study

Rui Dai, Gokul Chandrasekaran, Jie Chen, Chayton Jackson, Yongming Liu, Qiong Nian [*], Beomjin Kwon [**]

Department of Mechanical Engineering, School of Engineering for Matter, Transport and Energy, Arizona State University, Tempe, AZ, 85281, United States

ARTICLE INFO

ABSTRACT

Foams offer extremely large surface area per unit mass, making them competitive material for heat exchangers and energy storage systems. Understanding the influence of foam characteristics, i.e., size, distribution and concentration of pores, ligament defects as well as foam architecture, on thermal transport is important when designing the foam-based devices. In this article, we present the effective thermal conductivity of open-cell polyurethane (PU) foam (20 PPI) with ~10 μm thick nickel coating measured by transient plane source (TPS) method. A calibration methodology for TPS method is developed to obtain accurate measurements. A finite element model and thermal resistance model are developed for the heat transfer in metal coated foams occurring near room temperature. For precisely modeling the foam architecture topology, an X-Ray tomography is employed. The developed models are used to investigate how the Ni coating thickness affects the effective thermal conductivity. Lastly, we discuss how the model assumptions are related to the discrepancy between the model predictions and measurements for the polymer-metal foams.

1. Introduction

Due to the large surface area per unit mass and volume, porous media have received great interest for the energy device applications including thermal insulation [1], heat sinks [2], evaporators [3], heat exchangers [4–6], and energy storages [7,8]. Particularly, three-dimensional (3D) network architecture of foams was highlighted as the structures for supercapacitors and batteries, since these architectures serve as effective transport media for electrons and ions. Previous articles report that foams facilitate the electrolyte penetration into the electrode matrix, which possibly leads to overcoming the primary kinetic limits of the electrochemical process [9,10].

To properly design the porous media related to the thermal and energy applications, there has been extensive research to understand how the geometric parameters such as cell size and pore concentration affect the heat transfer modes and thermal conductivity (k). In gas-filled foams, dominant heat transfer modes are considered as solid conduction, gas conduction and radiation if the gas temperature is near or below the room temperature and the gas pressure is near or below the atmospheric pressure [11–13]. Natural convection is likely negligible in gas-filled foams especially if the cell sizes are less than 1 mm, as Rayleigh number (Ra) is much smaller than critical Ra (~40–1000) [11,13]. For instance, in an air-filled foam with a cell size of 1 mm, Ra is merely ~0.4 at room temperature. Another work reports that Darcy number (Da) is an important parameter to understand the onset of natural convection in foam [14]. With Da, Rayleigh number for porous media is defined as $Ra_m = RaDa\ k_f/k_m$, where k_f and k_m are the thermal conductivity of the fluid and saturated medium, respectively. If Ra_m exceeds 100, natural convection becomes important [14]. In closed-cell polyurethane (PU) foams with a cell sizes of 100–400 μm, the relative contributions of solid conduction, gas conduction and radiation were estimated as about 15, 70 and 15%, respectively at 286 K and 760 torr [12]. At a low pressure (<0.1 torr), the effective thermal conductivity (ETC) of foams reduced by 80% relative to the atmospheric condition owing to the absence of gas conduction [12].

To measure and study the thermal transport in porous media, various experimental methods have been explored. A standard approach is the guarded hot plate method which measures k under steady-state condition [15,16]. In this method, a hot plate dissipates a known unidirectional heat flux into the sample, which subsequently flows to a cold plate. The thermal conductivity is calculated from measured

* Corresponding author.,
** Corresponding author.
  E-mail addresses: qiong.nian@asu.edu (Q. Nian), kwon@asu.edu (B. Kwon).

Nomenclature

A	area [m²]		
Da	Darcy number		
D_T	mean deviation of ΔT [K]		
Fo	Fourier number		
H	distance between the top edge and bottom edge [m]		
k	thermal conductivity [W/(m·K)]		
l	strut length [m]		
l_w	strut width [m]		
L_i	height of each layer [m]		
Q	Joule heating [J]		
r	spiral radius [m]		
R	radius of the inscribed sphere [m]		
Ra	Rayleigh number		
T	temperature [K]		
V	volume [m³]		
V_i	volume of each layer envelope [m³]		

Greek letters

α	thermal diffusivity [mm²/s]
β	angle [°]
δ	probing depth [m]
ϕ	fraction of the solid phase

Subscripts

cond	conduction
cs	cross-section
eff	effective
f	fluid phase
m	saturated medium
Ni	nickel
PU	polyurethane
r	radius
s	solid phase (skeleton)
t	total
T	temperature

temperature gradient between the hot and cold plates. However, the steady-state method requires substantial measurement duration and extreme care in insultation. In recent studies [16,17], transient plane source (TPS) method is often employed, which only demands small-size samples, short measuring time and simple instrumentation relative to the steady-state method. The TPS method uses a thin metal film, sandwiched between two identical samples, to generate Joule heat, and records the transient temperature response of the samples to estimate the thermal conductivity. The TPS method measurements differed only about 20% from the steady-state technique measurements when tested for low-density, closed-cell polyethylene foams [16]. In another demonstration, TPS was used to measure k of PU foams where k was in the range of 0.048–0.05 W/(m·K) [17].

Theoretical models have also been proposed for the heat transfer in porous media. For simple modeling, foams are commonly treated as homogenous media consisting of solid matrix and fluid. Then, a one-dimensional (1D) heat conduction model has been set up to calculate the ETC of foams [18]. Although the 1D model predicts reasonably close to the experimental measurements, 3D numerical models have also been explored for accurate analysis by factoring in the actual foam structures [19]. For example, a previous work incorporated the actual morphologies of the porous medium obtained by 3D computed tomography (CT) scan for their numerical analysis [20].

Among various types of porous media, metal-polymer composite foams have attracted considerable interest due to their intriguing physical properties and competitive costs. If the porous medium merely consists of pure polymer foams, the structure generally possesses small k and poor mechanical strength, which are hard to be improved simply by altering the porous structure. To effectively modulate the thermal and mechanical properties of the foams, not only the architecture but also the constituent material needs to be engineered. For polymer foams, conformal metal coating on their ligament surface can be considered as a facile method of enhancing k and mechanical strength without large cost [21,22]. Metal coating on the polymer foams is usually implemented by a simple electrochemical co-deposition [23], which is scalable from nano-to-macro-scale sizes. However, to the best of our knowledge, only few studies [22,24] have investigated the thermal properties of such polymer metallic composite architecture despite their potentials and advantages.

This work reports the fabrication of Ni coated PU foams and measurement of their thermal conductivity using the TPS method. To understand the effect of Ni layer on thermal transport, a finite element model and a thermal resistance model are developed for the open-cell, composite foam. Herein, for the first time, we demonstrate that a

hollow pentagonal dodecahedron (HPD) model [25] can be used to effectively estimate the ETC of the composite foam. The HPD is adopted as a foam model to account for the realistic foam architecture. Although numerous FEM models have been developed for the foam architecture, including the Kelvin model [26], Weaire-Phelan model [27] and Tetrakaidecahedral model [28], these foam models are too complex to use for the foams with core-shell or hollow struts. X-ray tomography [29] is considered to provide an actual topology of the foam architecture, but it is still challenging to accurately capture the topology of thin coating layer and core material. For instance, the X-ray scanning is not able to measure the metal thickness. Consequently, the previous works based on X-ray scanning did not accurately account for the metal thickness or core structures of the composite foams [27,30,31]. It seems that the X-ray tomography model inevitably overpredicts the density of metal foam and overestimate the ETC of composite foams [20,32]. Alternatively, our 3D packing HPD model would provide a simple means to effectively approximate the composite foam architecture with core-shell or hollow struts.

2. Experiment

2.1. Sample fabrication by electroless-electrochemical deposition

Composite foams were prepared by coating Ni on reticulated PU foam templates (US Plastic Corp., OH) via the electroless-electrochemical deposition. Initially, the PU foams were cleaned with polyacetylene, acetone and deionized water alternatively in an ultrasonic bath for 20 min. Subsequently, the PU templates were immersed in dopamine·HCl solution with a concentration in the range of 1.0–3.0 g/L. The solution was in an open vessel (exposed to air) at room temperature and was stirred until the solution color changed from pink to brown (20 h). During the process, the solution was buffered at pH 8.5 by adding Tris. Then, the templates were washed with ethanol and deionized water alternately, and immersed in a copper electroless plating bath (Caswell Inc., NY). The copper plating was performed over 30 min to create conductive copper layer (~1 μm) on the template surface. Afterwards, ~10 μm-thick nickel layer was coated on top of the copper layer via pulse-reverse electrodeposition. For the nickel coating, complexing agents (310 g/L nickel sulfate, 35 g/L boric acid, 25 g/L nickel chloride, and 0.1 g/L saccharine) were prepared, and forward (0.1 A/cm²) and reverse (0.0015 A/cm²) currents were applied. After the deposition, the samples were inspected by using a scanning electron microscope (SEM, XL30, Phlips). Table 1 lists the open cell foams, i.e., polyethylene, polyurethane and nickel coated polyurethane foams, tested in this work

Table 1
Description of the test samples.

	Foam 1	Foam 2	Foam 3	Foam 4	Foam 5
Material	Polyurethane	Polyurethane	Polyurethane	Polyethylene	Ni/Cu/dopamine/polyurethane
Pore size, μm	494	105	247	263	635
Dimension, mm^3	$40 \times 40 \times 19$	$40 \times 40 \times 19$	$40 \times 40 \times 12.7$	$40 \times 40 \times 12.7$	$40 \times 40 \times 19$
Density, kg/m^3	23.35 ± 0.01	28.25 ± 0.01	48.45 ± 0.01	33.25 ± 0.01	42.39 ± 0.01
Strut thickness, μm	23 ± 1.3	12 ± 0.9	10 ± 0.5	2 ± 0.1	32 ± 1.5

with relevant properties including foam material, pore size, dimensions, density and the average strut thickness. Fig. 1(a–e) show the macroscopic images, and Fig. 1(f–j) show the microscopic images of the foams. To prepare Foam 5, Foam 1 was prepared, and additional layers were coated on Foam 1. For statistical reliability in measurements, 10 identical samples for each type of foam were prepared and tested.

2.2. Computed microtomography

To elucidate the foam architecture, we employed a high-resolution computed microtomography (μCT) system (SKYSCAN 1272, Bruker). The μCT system acquired a series of two-dimensional images of the foam through slice by slice scanning. The sliced image is denoted as layer throughout the article. To obtain the high-resolution anatomy of the foam, the sample was rotated 360° with a step of ~0.4° and five images were averaged to make each frame. The X-ray tube operated at an acceleration voltage of 70 kV with a spot size smaller than 5 μm. Finally, a conventional filtered back-projection algorithm was used to reconstruct the 3D foam model.

Fig. 2(a) shows the reconstructed model of the 3D composite foam while the inset image illustrates a representative layer. The layers were converted to contour images that only depict the foam strut boundaries as shown in Fig. 2(b). With the contour images, a sum of strut perimeters was calculated for each layer, denoted as total strut perimeter, using an open source image processing package (Fiji). Fig. 2(c) shows the total strut perimeter along the slice scanning direction which randomly fluctuates with an average of ~229.6 μm. Such fluctuating profile indicates the homogeneous and stochastic nature of the foam architecture.

With the μCT images, the cross-section areas of struts ($A_{PU,cs}$) and the nickel shell surrounding the struts ($A_{Ni,cs}$) were estimated. Due to the limited X-ray penetration depth and scanning resolution, the 3D anatomy model of a composite foam did not directly provide the nickel shell area. Thus, the nickel shell area was estimated by multiplying the total strut perimeter and nickel coating thickness. Through this method, $A_{Ni,cs}$ and $A_{PU,cs}$ were estimated as 3.44 mm^2 and 354 mm^2, respectively.

2.3. Transient plane source (TPS) method

The thermal conductivities of the foams were measured with TPS method at room temperature. Fig. 3(a) shows the measurement instrument (anisotropic module, TPS 2500 S, Thermtest, Inc). A sensor (C5501, Thermtest, Inc) included a spiral-shape, 10 μm-thick nickel foil, which was sandwiched by electrically insulating layers, 30 μm-thick polyimide (Kapton) film. The spiral area with a diameter of 12.8 mm generated Joule heating (Q), as the instrument supplied current over a predefined period of time (Δt). Sample width or diameter should be at least twice greater than the spiral diameter to ensure that the heat generated by the spiral area does not diffuse to the sample outside boundary within Δt. For the same reason, the sample thickness must be equal or greater than the spiral radius (r). Thus, we prepared foams with 40×40 mm^2 cross-sectional area and the thickness greater than 12.8 mm. For the measurements, two identical foams were brought into contact with the sensor and compressed by a screw. A proper amount of compression pressure was important to ensure consistent measurements and not to significantly deform the foam shape. After mounting the samples, the sensor generated heat Q, which was assumed to diffuse identically into two samples as illustrated in Fig. 3(b). Then, the instrument recorded the temporal change in electrical resistance of the nickel foil. The measured resistance was converted to sensor temperature based on a temperature coefficient of resistance. The thermal conductivity (k), was calculated from the inverse of the temperature increase (ΔT) per characteristic time constant, Fourier number *Fo*, using the following equation.
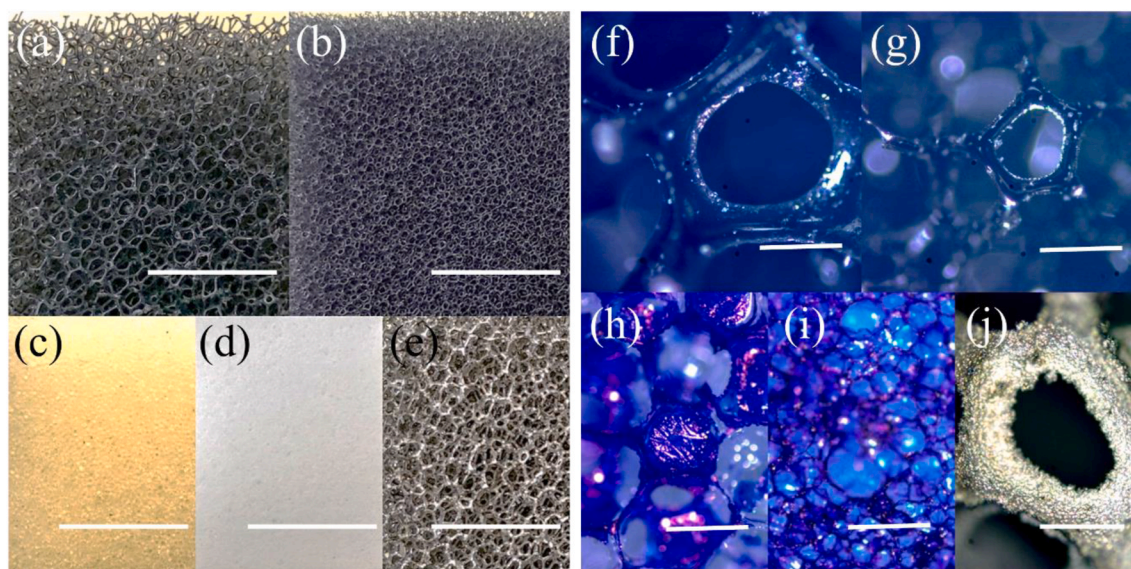

Fig. 1. Macroscopic and microscopic images of (a, f) Foam 1, (b, g) Foam 2, (c, h) Foam 3, (d, i) Foam 4, and (e, j) Foam 5. The scalebar represents 20 mm in the macroscopic images and 50 μm in the microscopic images.
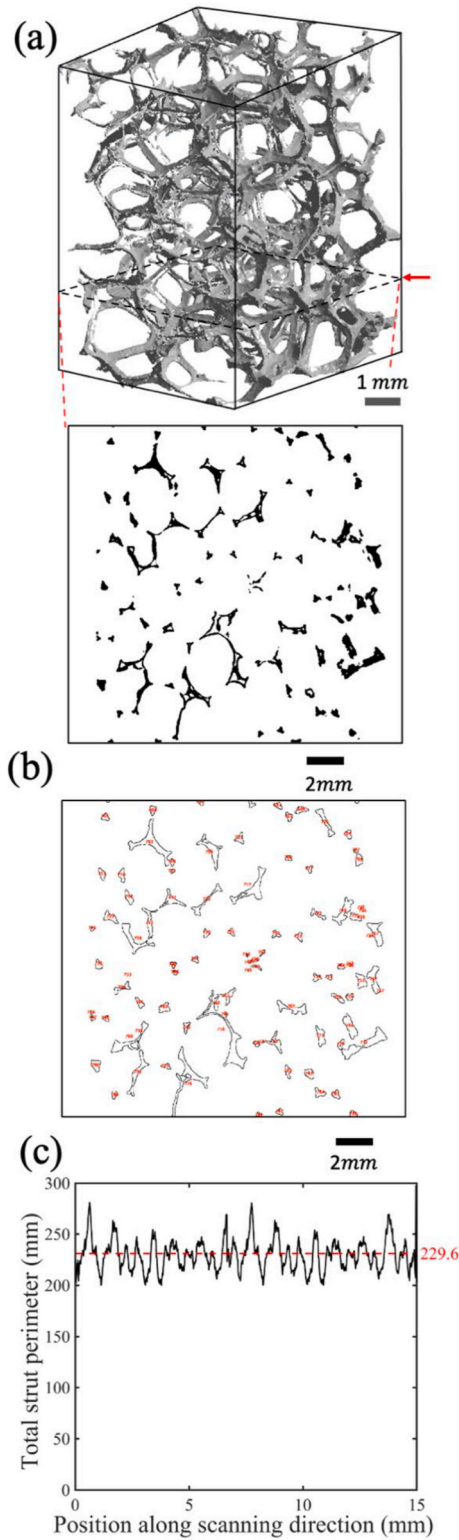
Fig. 2. (a) 3D rendering image of the nickel coated PU foam obtained by a static X-ray tomography system where the inset is the cross-section view for one selected layer. (b) A contour image indicating the strut boundary. (c) The total perimeter distribution of the foam from bottom to top surface. The red dash line indicates an average value (229.6 mm).
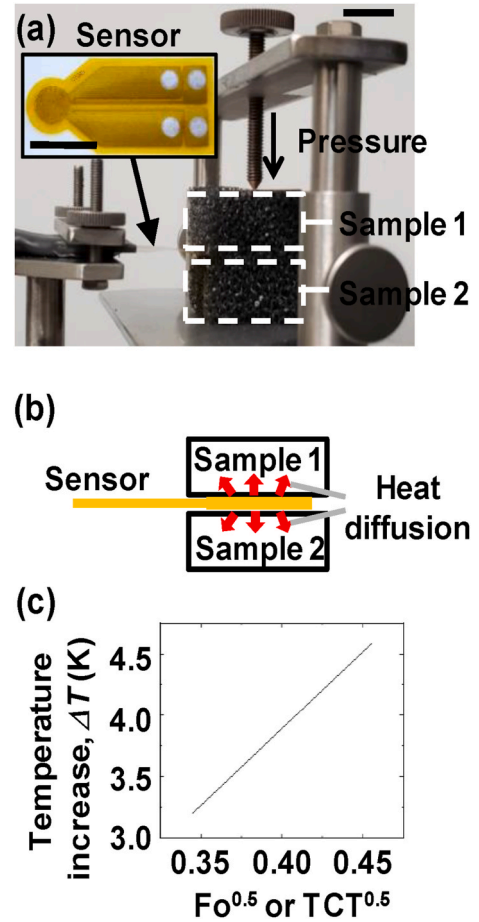

Fig. 3. TPS instrument for measuring the thermal conductivity of the samples: (a) photographic image (20 mm bar for scale), and (b) a schematic. (c) Temperature increase of the sensor as a function of the $Fo^{0.5}$ (equivalently $TCT^{0.5}$).

$$k = \frac{Q}{2\pi^{1.5}r} \frac{Fo^{0.5}}{\Delta T} \tag{1}$$

Fourier number is a dimensionless time constant defined as $\alpha \Delta t/r^2$, where α is the thermal diffusivity which is a function of k, density, and specific heat. Thus, Eq. (1) is an implicit equation for k, which is numerically solved based on multiple measurements of Δt and ΔT.

For an accurate and reliable measurements, two input parameters, Q and Δt, are critical, which, however, can only be chosen through trial-and-error approach. If Q is too small, temperature change is not measurable in high consistency. If Q is too large, sample temperature may excessively increase (e.g., $\Delta T > 5.5$ K), and the temperature dependence of thermal conductivity becomes nontrivial. Measurement time should also be adjusted for heat to diffuse sufficient depth into the sample, but not to penetrate through any sample boundary (e.g., 5 mm $\leq$ penetration depth $\leq$ 12 mm). To validate if Q and Δt are properly selected, TPS instrument estimates three validation metrics: radial probing depth (δ_r), a ratio of total measurement time to thermal characteristic time (TCT), and mean deviation of ΔT during measurements (D_T). The TCT is identically estimated as Fo, and recommended to be within the range of 0.33–1. During the measurement, ΔT is monitored as a function of the time constant $Fo^{0.5}$ as shown in Fig. 3(c), which typically presents a linear dependence of ΔT on $Fo^{0.5}$.

Fig. 4(a–c) show the validation metrics, δ_r, TCT, and D_T, as a function of the input parameters, Q and Δt, obtained with Foam 1. The range of Q was 10–40 mW and Δt ranged between 5 and 80 s. The validation metrics exhibited strong dependence on Δt. When $\Delta t > 20s$, δ_r reached the sample thickness and TCT exceeded 1, both indicating that heat
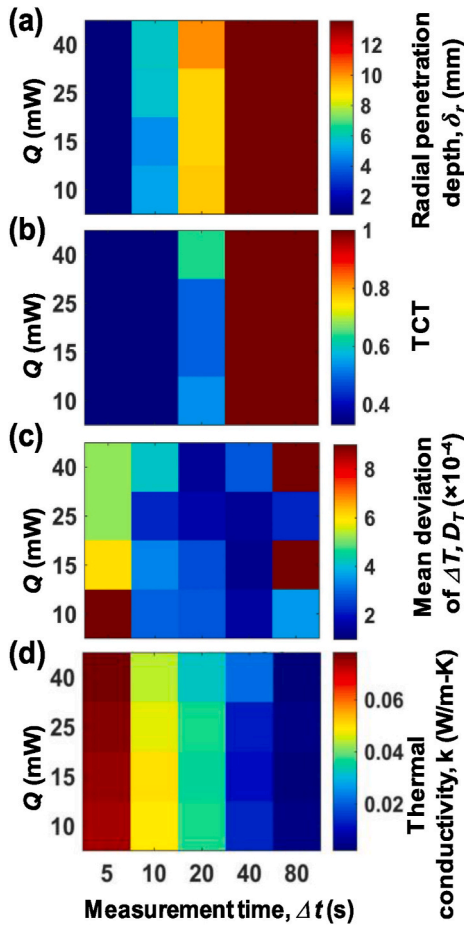
Fig. 4. (a–c) Validation metrics of TPS measurements as a function of input power and measuring time: (a) radial probing depth, δ_r, (b) TCT, and (c) mean deviation of ΔT, D_T. (d) Thermal conductivity measured for Foam 1.

excessively diffused. Thus, Δt was selected as 20s for a proper heat diffusion. When $Q > 40$ mW, the sample temperature increased greater than 5.5 K. When $Q < 10$ mW, ΔT was too small, e.g., $\Delta T < 1$ K. We also observed that the temperature fluctuated with greater D_T when a greater Q was employed, although D_T remained on the order of 10^{-4} in all the cases.

Fig. 4(d) is the measured k of Foam 1 as a function of Q and Δt. The measurement results significantly varied with Δt, changing from 0.01 W/(m·K) to 0.07 W/(m·K). The dependence of k on Q was small relative to the dependence on Δt. When $\Delta t > 20$s, k was considered under-estimated, as δ_r exceeded the sample boundary. When $\Delta t < 5$s, k was assumed incorrect, as the effect of thermal contact resistances was un-avoidable at the beginning of TPS measurements. Based on the corre-lations between the input parameters, validation metrics and k, we determined the ranges of Δt and Q for all foams as listed in Table 2. Properly selected Δt and Q ensured that 4 K $< \Delta T <$ 5.5 K, 0.33 < TCT <0.8, $\delta_r <$ sample length, and $D_T \ll 10^{-3}$.

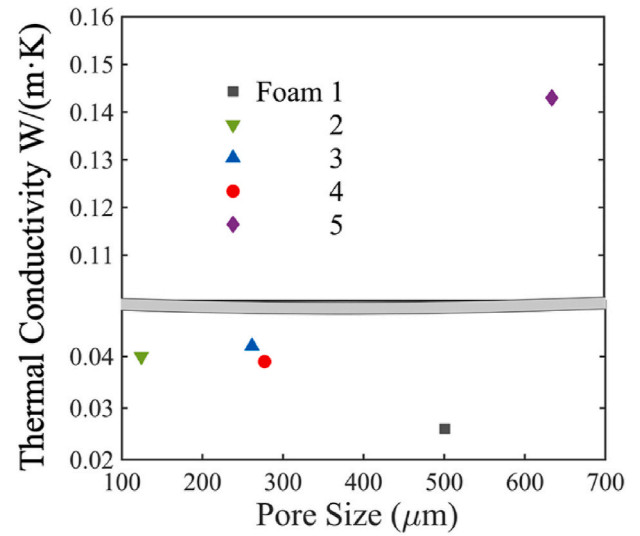Fig. 5 presents the TPS measurement results. To ensure the

Fig. 5. Thermal conductivity of the foams as a function of the pore size.

measurement reliability, each sample was measured 5 times. The ther-mal conductivities of the pure polymer foams (Foam 1–4) were extremely low and similar to k of air [0.026 W/(m·K)]. Particularly, k of Foams 2 and 3, pure PU foams, were close to each other as ~0.04 W/(m·K), although their pore sizes differed by a factor of 2. Foam 4, polyethylene foam, exhibited similar k to Foam 2–3 and to the value reported in a literature [33]. However, as the pores were enlarged to near 500 μm (Foam 1), k of PU foam reduced to 0.026 W/(m·K). On the other hand, the addition of Ni layer (Foam 5) enhanced k of Foam 1 by 5.5 times, confirming the contribution of the Ni layer.

The uncertainty in our measurements can be estimated from the observed variations of k as a function of Δt and Q as shown in Fig. 4. Within the selected ranges of Δt and Q, i.e., 5s $< \Delta t <$ 20s, 10 mW $< Q <$ 40 mW, the uncertainty in k was observed as approximately 0.03 W/(m·K). Thus, the uncertainty in our measurements is estimated at about 80% for the pure polymer foams (Foam 1–4) and 20% for the Ni coated foam (Foam 5). These uncertainties agree with the uncertainties esti-mated in the literature [34].

To understand if such augmentation in k was reasonable, we roughly estimated the effective thermal conductivity (ETC) of Foam 5 by using a simple 1D parallel heat conduction model. In this model, the foam was simplified as two parallel beams of PU and Ni with the same length. Then, the ETC of the foam was calculated with the following equation.

$$k_{eff} = \left(A_{PU,cs} / A_{cs}\right)k_{PU} + \left(A_{Ni,cs} / A_{cs}\right)k_{Ni}. \tag{2}$$

where A_{cs} is the total cross-section area of the foam structure which is equal to $A_{cs} = A_{PU,cs} + A_{Ni,cs}$. Considering the nanocrystalline (NC) na-ture of the electrochemically deposited nickel coating, k_{Ni} is assumed to be within the range of 67.3–78 W/(m·K) [35–37], which is smaller than the k of bulk nickel [90 W/(m·K)]. For this calculation, we used k of NC nickel at 300 K [76 W/(m·K)] [38]. Using Eq. (2), k_{eff} was estimated as 0.73 W/(m·K), which was ~5 times greater than the TPS measurement. A major possible reason of k_{eff} overestimation would be that Eq. (2) oversimplifies the foam geometry. In an actual foam, the path length of

Table 2
List of measurement parameters.

	Power Q, mW	Time Δt, s	Temperature increase ΔT, K	TCT	Probing depth δ_r, mm	Mean deviation D_T, 10^{-4}	Thermal conductivity k, W/(m·K)
Foam 1	20	20	4.68	0.71	6.89	4.80	0.026
Foam 2	20	20	4.43	0.398	7.66	1.85	0.040
Foam 3	20	20	5.17	0.402	8.22	2.91	0.042
Foam 4	15	40	4.17	0.392	8.26	1.87	0.039
Foam 5	20	10	4.38	0.445	13.8	3.29	0.143

thermal transport, which is a function of strut angular orientation, may be greatly different to the thermal transport path assumed in the 1D parallel heat conduction model. Furthermore, the overestimation of Eq. (2) can be partly ascribed to the defects formed in the nickel shell. Fig. 6 shows the SEM images of the nickel shell surface in Foam 5, indicating that the nickel coating is not perfectly continuous due to delamination, surface fracture and node fracture. Such defects would reduce $A_{Ni,cs}$. To account for the actual foam structure revealed by μCT images, we developed more realistic models in the following section.

3. Modeling

In this section, we develop a finite element model (FEM) and a thermal resistance model for the heat transfer in open-cell composite foams with several assumptions. As heat transfer mechanism, we only consider the conduction through the nickel skeleton due to the following reasons. Natural convection and radiation are neglected considering the fact that the total temperature increase is less than 6 K during the TPS measurements and the foam pore size is smaller than 1 mm [29]. Under this condition, Ra is estimated far less than 1. We further simplify the modeling by neglecting the heat conduction in air and PU struts, since k of air and PU are smaller than k_{Ni} by a factor of >5000.
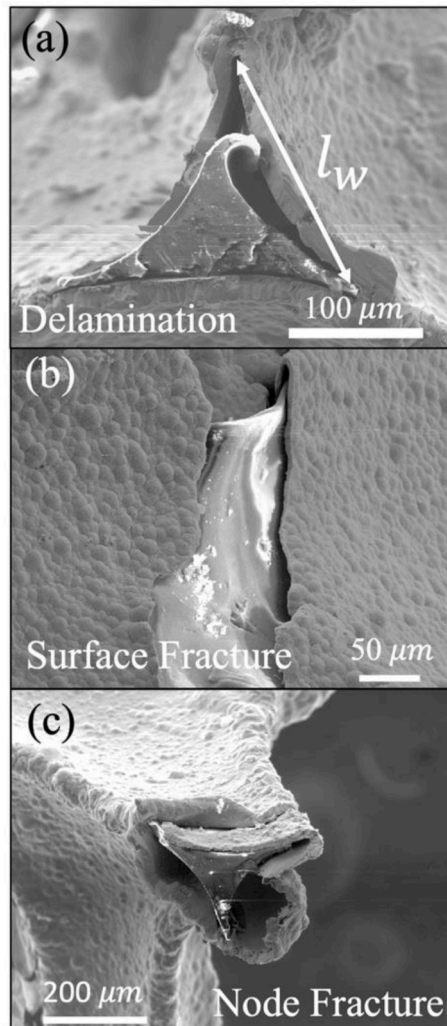
3.1. Finite element model

The FEM analysis (ANSYS 2019, R2) was carried out on the HPD model to simulate the temperature distribution of foam unit cell region. Fig. 7(a) presents the schematic of the HPD model with important geometric parameters including strut width (l_w), strut length (l), radius of the inscribed hole area (R), and edge-to-edge length (H). The pentagonal dodecahedron (PD) architecture, which has been employed as a geometric model of open-cell polymer foams [25,39], involves twenty nodes and thirty ligaments. In the HPD model, the inside space of the PD architecture or struts is hollow, mimicking the nickel shell of the composite foam. The calculated cross-section area of the HPD model fluctuates similar to the μCT 3D anatomy model, supporting that the HPD model resembles the actual foam architecture. Fig. 7(b) shows the cross-sectional area of an HPD model when a nickel coating thickness is 10 μm. In this particular HPD, the average cross-section area is 0.063 mm².

To calculate ETC, steady-state temperature distribution was

Fig. 6. SEM images of electro-plating defects found in Foam 5 including (a) delamination, (b) surface fraction and (c) node fracture.
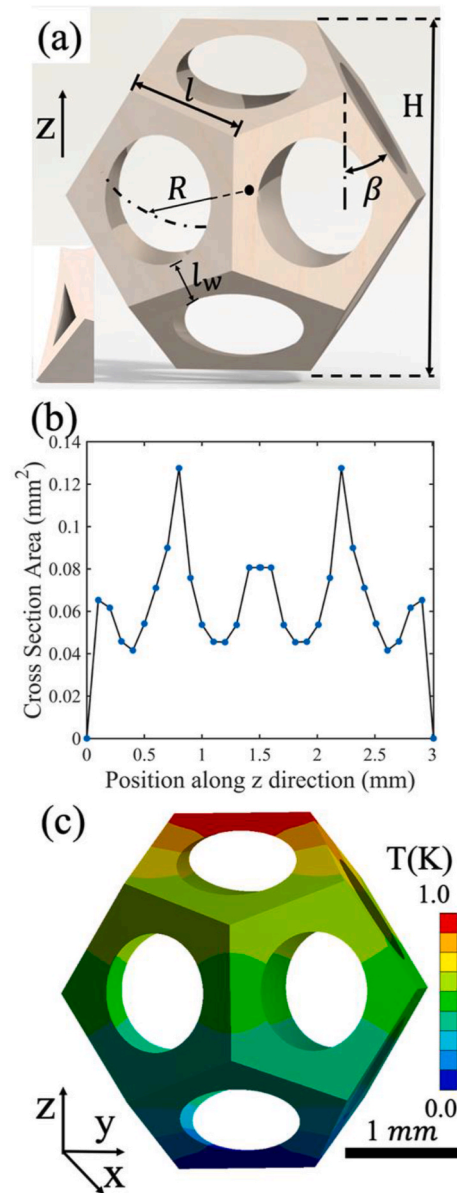

Fig. 7. (a) CAD model for a general PD structure; (b) Cross-section area distribution corresponding to the PD model in (b) with 10 μm nickel thickness; (c) Temperature contour plot computed with FEM simulation.

ARTICLE IN PRESS

R. Dai et al.   International Journal of Thermal Sciences xxx (xxxx) xxx

simulated with the FEM. As thermal boundary condition, temperature difference between two parallel ends of the HPD model was set to 1 K as shown in Fig. 7(c). The FEM employed the nickel properties at 300 K. To ensure mesh independent solution, fine adaptive mesh grids were generated with around 100,000 elements in the HPD model. The convergence threshold was set to 10^{-13} which was much lower than a default value 10^{-3} to ensure accurate solutions. Only considering the conduction rate through Ni shell (Q_{cond}), FEM calculated k_{eff} with the relation, $k_{eff} = Q_{cond}H/A_{Ni,cs}(T_{top} - T_{bottom})$, where T_{top} and T_{bottom} are the temperatures at the top and bottom edges. In this relation, $T_{top} - T_{bottom}$ was equal to 1 K, and $A_{Ni,cs}$ in the HPD model was equal to H^2. Thus, the above relation reduced to $k_{eff} = Q_{cond}/H$. For a comparison with the experiment results and another model to be developed, we calculated k_{eff} while varying the nickel thickness from 10 to 50 μm. Table 3 lists the relevant parameters and predicted k_{eff}.

3.2. Thermal resistance model

An analytical approach, thermal resistance model, was developed to investigate the influence of the strut angular distribution and thermal transport path length on the open-cell composite foam ETC. An analytical model enables to study the effect of a specific model parameter with reduced computation cost as compared to FEM. Many semi-analytical models were introduced in literatures [40–44] to estimate the foam ETC while modeling the foam architecture as a periodic lattice structure. We adopted the edge by edge 3D packing architecture which was compatible with the HPD foam model [25]. Fig. 8(a) shows the lattice structure consisting of $3 \times 3 \times 3$ HPD models.

In this approach, we divide the HPD lattice unit cell into 9 different layers and model them as a series of thermal resistances. Fig. 8(b) illustrates how the unit cell is divided along the z axis which corresponds to the heat transfer direction in the model. This layer division is based on the strut angular distribution such that the angle between the strut and z axis [β as indicated in Fig. 7(a)] may possess only one or two values in each layer. Accordingly, the height of each layer (L_i) can be expressed with l, l_w, and dihedral angle of 58.3° by using the relations below, where the subscript i indicates the order of layer.

$$L_1 = L_9 = \left(\sqrt{3}l_w \big/ 2\right)\cos 58.3^o \tag{3}$$

$$L_2 = L_8 = \left(l - \sqrt{3}\, l_w \big/ 2\right)\cos 18^o \cos 58.3^o \tag{4}$$

$$L_3 = L_7 = l \cos 72^o \cos 58.3^o \tag{5}$$

$$L_4 = L_6 = (l - l_w)/2 \tag{6}$$

$$L_5 = l_w \tag{7}$$

The ETC of the open cell foam is often estimated using the volume averaged method [45], which can also be used to model the ETC of unit cell layers. Then the ETC of each layer ($k_{i,eff}$) is modeled as below [42].

Table 3
HPD lattice model parameters and results.

| Ni thickness (μm)	Q_{cond} (mW)	l_w (μm)	V_t (mm³)	L (mm)	H (mm)	k_{eff}, FEM [W/(m·K)]	k_{eff}, Eq. (14) [W/(m·K)]
10	0.514	214.5	0.196	1.150	3.01	0.171	0.154
15	0.830	234.5	0.311	1.154	3.02	0.275	0.247
20	1.14	254.5	0.436	1.159	3.03	0.377	0.354
25	1.50	274.5	0.573	1.163	3.04	0.492	0.468
30	1.88	294.5	0.710	1.167	3.06	0.615	0.588
35	3.07	314.5	0.868	1.172	3.07	0.745	0.727
40	3.08	334.5	1.04	1.177	3.08	0.884	0.878
45	3.09	354.5	1.22	1.181	3.09	1.026	1.041
50	3.10	374.5	1.41	1.185	3.10	1.192	1.217
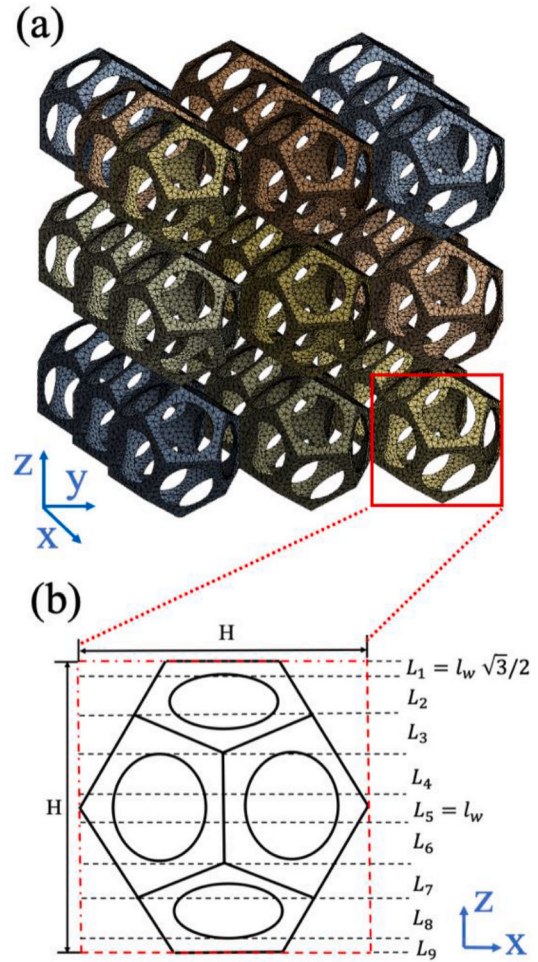
Fig. 8. (a) Schematic diagram of the 3D packing HPD lattice architecture. (b) A representative unit volume, which is divided into 9 different layers considering the strut orientation.

$$k_{i,eff} = \phi k_s \cos^2 \beta + (1 - \phi)k_f \tag{8}$$

where k_s is the thermal conductivity and ϕ is the volume fraction of the solid skeleton. In Eq. (8), the second term on the right-hand side is assumed negligible, because $k_s \gg k_f$. Then, based on the strut angular orientations of each layer, $\cos\beta$ is determined as follows. For layers 1 and 8, $\cos\beta = 1$. For layers 2 and 7, $\cos\beta = \cos 18^\circ \cos 58.3^\circ$. For layers 3 and 6, $\cos\beta = \cos 72^\circ \cos 58.3^\circ$. For layers 4 and 5, $\cos\beta$ is 1 for the orthogonal struts and $\cos 18^\circ \cos 58.3^\circ$ for the tilted strut. The volume fraction ϕ is calculated by the strut volume divided by the layer envelope volume (V_i), where $V_i = L_i H^2$.

Considering that the struts can be shared by more than one unit cell in lattice, the number and volume of struts are determined as follows. Layers 1 and 9 include 1 complete horizontal strut each. Layers 2 and 8 include $4(l - l_w)\cos 18^\circ \cos 58.3^\circ$ struts each. In layers 3 and 7, there are 4 + $4(1 - \varepsilon)$ struts in total, where $\varepsilon = 0.5l/(0.5H - l \cos 18^\circ \cos 58.3^\circ)$. In layers 4 and 6, there are $(l - l_w) + 4(\varepsilon - l_w/l)$ struts in total. Layer 5 includes $2 + 2l_w/l$ struts. Thus, each unit cell possesses 30 struts in total. If the volume of a single strut is expressed as $V_t/30$, where V_t is the total volume of struts per unit cell, then $k_{i,eff}$ is obtained as below.

$$k_{1,eff} = k_{9,eff} = \frac{1}{30}\frac{V_t}{V_1}k_s \tag{9}$$

$$k_{2,eff} = k_{8,eff} = \frac{2}{15}\frac{V_t}{V_2}k_s(\cos 18^o \cos 58.3^o)^2\, k_s \tag{10}$$
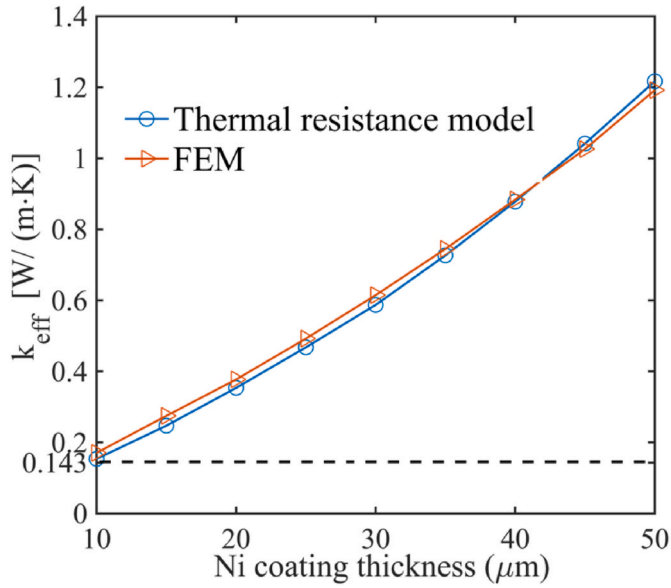
Fig. 9. The ETC of the HPD architecture predicted by FEM and the thermal resistance model as a function of Ni coating thickness. The black dash line indicates our experiment result, corresponding to ETC = 0.143 W/(m·K). The Ni coating thickness of experimental samples is approximately 10 μm.

$$k_{3,eff} = k_{7,eff} \tag{11}$$

$$k_{4,eff} = k_{6,eff} = \frac{1}{30} \frac{V_t}{V_4} \frac{l - l_w}{l} k_s + \frac{2}{15} \left(\varepsilon \frac{V_t}{V_4} - \frac{l_w}{l} \frac{V_t}{V_4} \right) (\cos 18^o \cos 58.3^o)^2 k_s \tag{12}$$

$$k_{5,eff} = \frac{1}{15} \frac{l_w}{l} \frac{V_t}{V_5} k_s + \frac{1}{15} \frac{V_t}{V_5} k_s \tag{13}$$

For the thermal resistances in series, the total thermal resistance is the sum of constituents. Accordingly, the ETC of an HPD unit cell is obtained as below.

$$k_{eff} = H \left/ \left[\frac{2(l_w\sqrt{3}/2)\cos58.3^o}{k_{1,eff}} + \frac{2(l - l_w)\cos18^o \cos58.3^o}{k_{2,eff}} + \frac{2l\cos72^o \cos58.3^o}{k_3,eff} + \frac{(l - l_w)/2}{k_{4,eff}} + \frac{l_w}{k_{5,eff}} \right] \right. \tag{14}$$

Table 3 lists the predicted k_{eff} by Eq. (14).

4. Discussion

The comparison between model predictions indicates that the consideration of strut angular distribution and thermal transport path length is important for modeling the ETC of foams. We first cross-validated FEM and the thermal resistance model by comparing their predictions for various nickel coating thicknesses. Fig. 9 shows that k_{eff} of the composite foam estimated by FEM and the thermal resistance model are sufficiently close to each other. Especially, for 10 μm coating thickness, both models predict similar to the experimentally measured k [0.143 W/(m·K)], whereas the simple 1D parallel heat conduction model (Eq. (2)) overpredicts k_{eff} as 0.73 W/(m·K). This result supports that the foam architecture is a critical factor in foam ETC modeling, which is also intuitively reasonable considering the fact that heat flows through highly curved and long passages in actual foams when

conduction is a dominant heat transfer mode. Still, the models based on HPD foam architecture slightly overestimate k_{eff} about 10–15%. Possible reasons for the model errors would be the inaccuracies in thickness and thermal conductivity of nickel shell, coating defects and the difference between the HPD 3D-packing architecture model and actual foam architecture. However, the models based on HPD foam architecture do not seem oversimplify the actual foam architecture when considering their predictions of k_{eff} and foam cross-section area, thus they can be considered as valid and facile tools for modeling composite foams.

5. Conclusions

This work investigated the thermal conductivity of the metal coated polymer composite foam based on TPS measurements and modeling. The ~10 μm thick nickel coated open-cell PU foams exhibited k_{eff} of 0.143 W/(m·K), which was 5.5 folds improvement against pure PU foams. To understand the k_{eff} enhancement in the composite foam, a FEM and thermal resistance model were developed based on the recently proposed HPD 3D-packing architecture. The comparison between the experimental measurement and models clearly revealed the influence of the foam architecture, i.e., strut angular distribution and thermal transport path length, on the ETC of the foam-based architecture. When simplifying the composite foam as parallel beam conductors, the model prediction overestimated the thermal conductivity by a factor of 5. On the contrary, the models based on HPD foam architecture predicted close to the experimental measurement, supporting that the foam architecture is a critical factor for modeling ETC. The developed analytical model exhibited similar accuracy to FEM, validating that it is a new facile method to approximate the ETC of the open cell composite foam as a function of foam porosity and geometrical parameters.

The heat transfer enhancement in polymer foams by thin nickel coating would find applications in polymer heat exchangers and catalyst devices. Polymer heat exchangers have been popularly used in corrosive environment, but small thermal conductivities and poor mechanical properties have limited their applications. The nickel-coated polymer foam can be used to construct mechanically strong and highly thermally conductive structures. Fortunately, nickel is corrosion-resistive to many kinds of fluid. Moreover, the high thermal conductivity of the composite foams is useful to achieve a uniform temperature distribution in catalysis

devices that are made of polymer foams. Equalizing the temperature distribution is critical for the catalyst devices and can help to improve their overall efficiency [46]. The nickel coated polymer foams are also electrically conductive and possess large surface areas, thus thy can be used to make supercapacitors electrodes [47], oil absorption media [48], and electromagnetic interference shields [49].

References

[1] X. Yang, S. Feng, Q. Zhang, Y. Chai, L. Jin, T.J. Lu, The role of porous metal foam on the unidirectional solidification of saturating fluid for cold storage, Appl. Energy 194 (2017) 508–521.

[2] W.H. Shih, W.C. Chiu, W.H. Hsieh, Height effect on heat-transfer characteristics of aluminum-foam heat sinks, J. Heat Tran. 128 (2005) 530–537.

[3] G.B. Abadi, K.C. Kim, Enhancement of phase-change evaporators with zeotropic refrigerant mixture using metal foams, Int. J. Heat Mass Tran. 106 (2017) 908–919.

[4] T.J. Lu, H.A. Stone, M.F. Ashby, Heat transfer in open-cell metal foams, Acta Mater. 46 (1998) 3619–3635.

[5] K. Boomsma, D. Poulikakos, F. Zwick, Metal foams as compact high performance heat exchangers, Mech. Mater. 35 (2003) 1161–1176.

[6] A. Ejlali, A. Ejlali, K. Hooman, H. Gurgenci, Application of high porosity metal foams as air-cooled heat exchangers to high heat load removal systems, Int. Commun. Heat Mass 36 (2009) 674–679.

[7] Y. Zhong, Q. Guo, S. Li, J. Shi, L. Liu, Heat transfer enhancement of paraffin wax using graphite foam for thermal energy storage, Sol. Energy Mater. Sol. Cells 94 (2010) 1011–1014.

[8] C.Y. Zhao, W. Lu, Y. Tian, Heat transfer enhancement for thermal energy storage using metal foams embedded within phase change materials (PCMs), Sol. Energy 84 (2010) 1402–1412.

[9] K.I. Siwek, S. Eugénio, D.M.F. Santos, M.T. Silva, M.F. Montemor, 3D nickel foams with controlled morphologies for hydrogen evolution reaction in highly alkaline media, Int. J. Hydrogen Energy 44 (2019) 1701–1709.

[10] L. Hou, Y. Shi, C. Wu, Y. Zhang, Y. Ma, X. Sun, J. Sun, X. Zhang, C. Yuan, Monodisperse metallic NiCoSe2 hollow sub-microspheres: formation process, intrinsic charge-storage mechanism, and appealing pseudocapacitance as highly conductive electrode for electrochemical supercapacitors, Adv. Funct. Mater. 28 (2018) 1705921.

[11] C.-j. Tseng, M. Yamaguchi, T. Ohmori, Thermal conductivity of polyurethane foams from room temperature to 20 K, Cryogenics 37 (1997) 305–312.

[12] J.-W. Wu, W.-F. Sung, H.-S. Chu, Thermal conductivity of polyurethane foams, Int. J. Heat Mass Tran. 42 (1999) 2211–2217.

[13] D.J. Close, J.G. Symons, R.F. White, Convective heat transfer in shallow, gas-filled porous media: experimental investigation, Int. J. Heat Mass Tran. 28 (1985) 2371–2378.

[14] C.Y. Zhao, T.J. Lu, H.P. Hodson, Natural convection in metal foams with open cells, Int. J. Heat Mass Tran. 48 (2005) 2452–2463.

[15] D. Salmon, Thermal conductivity of insulations using guarded hot plates, including recent developments and sources of reference materials, Meas. Sci. Technol. 12 (2001) R89.

[16] O. Almanza, M.A. Rodríguez-Pérez, J.A. De Saja, Applicability of the transient plane source method to measure the thermal conductivity of low-density polyethylene foams, J. Polym. Sci. B Polym. Phys. 42 (2004) 1226–1234.

[17] D.S.W. Pau, C.M. Fleischmann, M.J. Spearpoint, K.Y. Li, Thermophysical properties of polyurethane foams and their melts, Fire Mater. 38 (2014) 433–450.

[18] M.A.A. Mendes, S. Ray, D. Trimis, A simple and efficient method for the evaluation of effective thermal conductivity of open-cell foam-like structures, Int. J. Heat Mass Tran. 66 (2013) 412–422.

[19] R. Coquard, D. Baillis, Numerical investigation of conductive heat transfer in high-porosity foams, Acta Mater. 57 (2009) 5466–5479.

[20] C. Petit, E. Maire, S. Meille, J. Adrien, Two-scale study of the fracture of an aluminum foam by X-ray tomography and finite element modeling, Mater. Des. 120 (2017) 117–127.

[21] D.L. Burris, W.G. Sawyer, Hierarchically constructed metal foam/polymer composite for high thermal conductivity, Wear 264 (2008) 374–380.

[22] P.S. Liu, H.B. Qing, H.L. Hou, Y.Q. Wang, Y.L. Zhang, EMI shielding and thermal conductivity of a high porosity reticular titanium foam, Mater. Des. 92 (2016) 823–828.

[23] A. Torrents, T.A. Schaedler, A.J. Jacobsen, W.B. Carter, L. Valdevit, Characterization of nickel-based microlattice materials with structural hierarchy from the nanometer to the millimeter scale, Acta Mater. 60 (2012) 3511–3523.

[24] X.-H. Han, Q. Wang, Y.-G. Park, C. T'joen, A. Sommers, A. Jacobi, A review of metal foam and metal matrix composites for heat exchangers and heat sinks, Heat Tran. Eng. 33 (2012) 991–1009.

[25] R. Dai, M. Wang, D. Wang, Z. Hu, M.D. Green, Q. Nian, Understanding mechanical behavior of metallic foam with hollow struts using the hollow pentagonal dodecahedron model, Scripta Mater. 182 (2020) 114–119.

[26] W.E. Warren, A.M. Kraynik, Linear elastic behavior of a low-density Kelvin foam with open cells, J. Appl. Mech. 64 (1997) 787–794.

[27] K. Boomsma, D. Poulikakos, Y. Ventikos, Simulations of flow through open cell metal foams using an idealized periodic cell structure, Int. J. Heat Fluid Flow 24 (2003) 825–834.

[28] Y.W. Kwon, R.E. Cooke, C. Park, Representative unit-cell models for open-cell metal foams with or without elastic filler, Mater. Sci. Eng., A 343 (2003) 63–70.

[29] Y. Amani, A. Takahashi, P. Chantrenne, S. Maruyama, S. Dancette, E. Maire, Thermal conductivity of highly porous metal foams: experimental and image based finite element analysis, Int. J. Heat Mass Tran. 122 (2018) 1–10.

[30] M. Wang, N. Pan, Modeling and prediction of the effective thermal conductivity of random open-cell porous foams, Int. J. Heat Mass Tran. 51 (2008) 1325–1331.

[31] X. Xiao, P. Zhang, M. Li, Effective thermal conductivity of open-cell metal foams impregnated with pure paraffin for latent heat storage, Int. J. Therm. Sci. 81 (2014) 94–105.

[32] L. Salari-Sharif, S.W. Godfrey, M. Tootkaboni, L. Valdevit, The effect of manufacturing defects on compressive strength of ultralight hollow microlattices: a data-driven study, Additive Manufacturing 19 (2018) 51–61.

[33] J.A. Martinez-Diez, M.A. Rodríguez-Pérez, J.A. De Saja, L.O. Arcos y Rábago, O. A. Almanza, The thermal conductivity of a polyethylene foam block produced by a compression molding process, J. Cell. Plast. 37 (2001) 21–42.

[34] Q. Zheng, S. Kaur, C. Dames, R.S. Prasher, Analysis and improvement of the hot disk transient plane source method for low thermal conductivity materials, Int. J. Heat Mass Tran. 151 (2020) 119331.

[35] H.J. Cho, S. Wang, Y. Zhou, G. Palumbo, U. Erb, Thermal conductivity of bulk electrodeposited nanocrystalline nickel, Int. J. Heat Mass Tran. 100 (2016) 490–496.

[36] R.A. Sayer, J. Zeng, H.-H. Hsu, D. Peroulis, T.S. Fisher, Thermal and electrical conductivities of nanocrystalline nickel microbridges, J. Microelectromech. Syst. 21 (2012) 850–858.

[37] H.J. Cho, J. Tam, M. Kovylina, Y.-J. Kim, U. Erb, Thermal conductivity of bulk nanocrystalline nickel-diamond composites produced by electrodeposition, J. Alloys Compd. 687 (2016) 570–578.

[38] S. Wang, Thermal Conductivity of Nanocrystalline Nickel, University of Toronto, 2011.

[39] T.T. Huu, M. Lacroix, C.P. Huu, D. Schweich, D. Edouard, Towards a more realistic modeling of solid foam: use of the pentagonal dodecahedron geometry, Chem. Eng. Sci. 64 (2009) 5131–5142.

[40] V.V. Calmidi, R.L. Mahajan, The effective thermal conductivity of high porosity fibrous metal foams, J. Heat Tran. (1999) 121.

[41] K. Boomsma, D. Poulikakos, On the effective thermal conductivity of a three-dimensionally structured fluid-saturated metal foam, Int. J. Heat Mass Tran. 44 (2001) 827–836.

[42] Z. Dai, K. Nawaz, Y.G. Park, J. Bock, A.M. Jacobi, Correcting and extending the Boomsma–Poulikakos effective thermal conductivity model for three-dimensional, fluid-saturated metal foams, Int. Commun. Heat Mass 37 (2010) 575–580.

[43] X.H. Yang, J.X. Bai, H.B. Yan, J.J. Kuang, T.J. Lu, T. Kim, An analytical unit cell model for the effective thermal conductivity of high porosity open-cell metal foams, Transport Porous Media 102 (2014) 403–426.

[44] D. Baillis, R. Coquard, S. Cunsolo, Effective conductivity of Voronoi's closed-and open-cell foams: analytical laws and numerical results, J. Mater. Sci. 52 (2017) 11146–11167.

[45] M. Kaviany, Principles of Heat Transfer in Porous Media, Springer Science & Business Media, 2012.

[46] R.M. Heck, S. Gulati, R.J. Farrauto, The application of monoliths for gas phase catalytic reactions, Chem. Eng. J. 82 (2001) 149–156.

[47] R. Li, S. Wang, Z. Huang, F. Lu, T. He, NiCo2S4@ Co (OH) 2 core-shell nanotube arrays in situ grown on Ni foam for high performances asymmetric supercapacitors, J. Power Sources 312 (2016) 156–164.

[48] H. Shi, D. Shi, L. Yin, Z. Yang, S. Luan, J. Gao, J. Zha, J. Yin, R.K.Y. Li, Ultrasonication assisted preparation of carbonaceous nanoparticles modified polyurethane foam with good conductivity and high oil absorption properties, Nanoscale 6 (2014) 13748–13753.

[49] W. Yang, S. Luo, B. Zhang, Z. Huang, X. Tang, Electroless preparation and characterization of magnetic Ni–P plating on polyurethane foam, Appl. Surf. Sci. 254 (2008) 7427–7430.